Amorphous Ge-Sb-Se-Te chalcogenide films fabrication for potential environmental sensing and nonlinear photonics

T. Halenkovič, M. Baillieul, J. Gutwirth, P. Nemec, V. Nazabal

To cite this version:

T. Halenkovič, M. Baillieul, J. Gutwirth, P. Nemec, V. Nazabal. Amorphous Ge-Sb-Se-Te chalcogenide films fabrication for potential environmental sensing and nonlinear photonics. Journal of Materiomics, 2022, 8 (5), pp.1009-1019. ⟨10.1016/j.jmat.2022.02.013⟩. ⟨hal-03780187⟩

HAL Id: hal-03780187
https://hal.science/hal-03780187v1

Submitted on 23 Nov 2022

Amorphous Ge-Sb-Se-Te chalcogenide films fabrication for potential environmental sensing and nonlinear photonics

Tomáš Halenkovič[1,2], *Marion Baillieul*[2,1], *Jan Gutwirth*[1], *Petr Němec*[1] *and Virginie Nazabal*[2,1]*

[1]Department of Graphic Arts and Photophysics, Faculty of Chemical Technology, University of Pardubice, Studentská 573, 53210 Pardubice, Czech Republic

[2]Univ Rennes, CNRS, ISCR (Institut des Sciences Chimiques de Rennes) – UMR 6226, F-35000 Rennes, France

*Corresponding author: virginie.nazabal@univ-rennes1.fr

Abstract

Quaternary Ge-Sb-Se-Te chalcogenide thin films were fabricated by rf magnetron sputtering from $Ge_{19}Sb_{17}Se_{64-x}Te_x$ (x=5, 10, 15, 20) sputtering targets in order to select appropriate compositions for infrared sensor and optical nonlinear applications. An influence of chemical composition and deposition parameters on the optical properties, structure and wettability was thus studied. The amorphous thin films seem to be constituted by selenide entities that can include tellurium atoms in variable proportion such as $[GeSe_{4-x}Te_x]$ and $[SbSe_{3-x}Te_x]$ (x = 0, 1, 2) and Ge(Sb)-Ge(Sb) bonds according to Raman spectroscopy. Contact angle measurements of the thin films showed values of 68–71° for water and their surface energies in the range of ~36–39 $mJ{\cdot}m^{-2}$ seem suitable for surface functionalization required for photonic sensor development. Furthermore, the maximum nonlinearity at the telecom wavelength with respect to the highest figure of merit value was found for the thin film with composition $Ge_{19}Sb_{17}Se_{56}Te_8$ having nonlinear refractive index of 28×10^{-18} $m^2{\cdot}W^{-1}$. Due to their low optical bandgap energies, they may find their full interest for nonlinear optics in the mid-infrared range. Wide IR transparency in combination with high (non)linear refractive indices make these materials attractive in the field of mid-IR sensing and optical nonlinear devices.

Keywords

chalcogenide, thin films, glass, amorphous, optical properties, NLO, contact angles, sputtering, Raman

1. Introduction

Amorphous chalcogenides, non-crystalline solids based on the elements of chalcogens (*i.e.* S, Se, Te), are well known for their unique properties such as low phonon energies resulting in broad transmission window, photoinduced phenomena or high optical nonlinearities without free carriers [1-3]. These make them suitable for potential applications in various fields including phase-change materials [4], artificial neural networks [5], non-linear photonics [3], optical sensors [6], mid-IR sources [7] *etc*.

Indeed, with the addition of a third element such as Sb to the Ge-Se binary system, the glassy material is stabilized by cross-links between more diverse structural entities that create configurational changes in the system, which could promote the broadening of the glass formation domain and influence the physical properties [8]. In detail, when a small amount of Sb is added to Ge–Se system, a significant decrease in optical loss can be observed [9]. Previously, Ge-Sb-Se (herein GSS) based infrared sensor devoted to evanescent wave detection was designed and fabricated [6]. The transducer was made of two superposed amorphous thin layers. The cladding and guiding layers were of $Ge_{31}Sb_6Se_{62}$ and $Ge_{15}Sb_{24}Se_{61}$ for the real compositions of the sputtered thin films deposited at 1×10^{-2} mbar and 20 W and 10 W, respectively and presenting a refractive index contrast of 0.33±0.02 at 7.7 µm [10]. Even if these two compositions have allowed the realization of efficient optical waveguides for sensor [6] and nonlinear optical applications [11], $Ge_{12.5}Sb_{25}Se_{62.5}$ glass targets used for thin film sputtering are less resistant to thermomechanical stresses than $Ge_{28.1}Sb_{6.3}Se_{65.6}$ ones. This induces a high material loss during the various stages of glass target fabrication.

Causing higher financial and temporal cost, the authors were interested in finding a pair of compositions that also meet the criteria necessary for the fabrication of a waveguide for integrated optics, while being more robust from thermomechanical point of view. The $(GeSe_2)$-(Sb_2Se_3) pseudo-binary system has been previously studied by Olivier *et al.* [12]. Subsequently, it was found that the particular composition of $Ge_{19.4}Sb_{16.7}Se_{63.9}$ for the glass target, that corresponds to $(GeSe_2)_{70}(Sb_2Se_3)_{30}$, is suitable for natural water pollution detection sensors in mid-IR region [13] as well as for nonlinear photonics devices limiting two photon absorption at 1.55 µm from $0.37\ \mathrm{cm} \cdot \mathrm{GW}^{-1}$ for slab waveguide and photosensitivity related to optical nonlinearity effects [12, 14]. Nevertheless, the refractive index contrast of the mid-IR waveguide was lower due to mentioned composition change, with a refractive index contrast of $\Delta n = 0.21 \pm 0.02$ at 7.7 µm between the buffer ($Ge_{31}Sb_6Se_{63}$) and the guiding ($Ge_{22}Sb_{16}Se_{62}$) layers deposited at an Ar pressure of 5×10^{-3} mbar and RF power at 15 W [13].

The linear and nonlinear refractive index contrast would be increased by a substitution of tellurium to selenium. Quaternary Ge-Sb-Se-Te alloys also known as GSST have already attracted the attention of some authors [15-18]. First, it is considered to be a promising replacement of $Ge_2Sb_2Te_5$ for high-performance phase-change material applications due to the higher 10-year data retention as reported by Wang *et al.* [17]. Moreover, the substitution of selenium by heavier tellurium atoms causes the decrease of lattice phonon energies broadening the transparency within mid-IR region. Thus, Te-based glasses present extended transmission in the 6–20 µm range and consequently allow the detection of the greenhouse gases absorption peaks especially at longer wavelengths than usual [19, 20]. Besides that, an increasing tellurium concentration causes the rise of the linear refractive index making GSST promising materials for nonlinear optical applications [15].

In this work, the influence of chemical composition and deposition parameters on the optical properties, structure and wettability of the GSST thin films was studied and the potential application of GSST thin film for mid-IR sensing and nonlinear optical (NLO) applications is discussed.

2. Materials and methods

Glass-ceramics sputtering targets having compositions of $Ge_{19}Sb_{17}Se_{64-x}Te_x$ (x = 5, 10, 15, 20) were obtained by a conventional melt-quenching technique. The maximum concentration of tellurium in the GSST targets was limited by the feasibility of fabricating sputtering targets of 50 mm diameter and 3.5 mm thickness. The thermal analysis of the bulk targets was performed at $10\ °\mathrm{C}.\ \mathrm{min}^{-1}$ by means of differential scanning calorimetry (DSC, TA Instruments DSC Q20, USA). Bulk material obtained from targets' synthesis was also used for further analysis in order to investigate potential crystallinity of sputtering targets. The X-ray diffraction (XRD) data were recorded with a X'Pert Pro Malvern Panalytical diffractometer (Cu Kα, 2θ: 5°-90°, step size: 0.026°, step time: 40s, voltage: 40kV, current: 40mA).

Thin films were deposited at a room temperature by rf (13.56 MHz) magnetron sputtering in Ar plasma. The substrates used for the deposition were borosilicate glass (Schott, BK7) and single crystalline silicon <100>. The former was used for spectrometric and X-ray diffraction (XRD) measurements, the later for scanning electron microscopy with energy-dispersive X-ray analyser (SEM-EDS), atomic force microscopy (AFM) and the contact angle measurements. The electrical power applied on targets was 10 and 15 W. Two different Ar pressures were maintained in the deposition chamber, specifically 5×10^{-3} and 1×10^{-2} mbar, while the Ar flow was kept constant (*i.e.* 75 sccm). In order to be able to characterize the surface of the GSST thin films by AFM or contact angle techniques, they were kept in a desiccator in the dark because whatever the composition of the layer, the impact of visible light and UV as well as the moisture on the thin layers is documented and has to be minimized [21]. In case of both, the contact angle measurements as well as AFM, experiments are carried out with a minimum time delay after the deposition of thin films. Routinely, spectroscopic ellipsometry and AFM are performed with a highest priority compared to other experiments.

Topography of fabricated films was measured by amplitude modulated AFM (Solver Next, NT-MDT, Russia). Furthermore, chemical composition of thin films was obtained from EDS analysis using joint SEM-EDS (JEOL IT 300 LA EDS, JEOL Ltd., Japan). EDS (ZAF standardless method) remains a relatively imprecise measurement as evidenced by its expected uncertainty (±1 at. %) especially for thin films where the contribution of the substrate can become significant. However, in similar acquisition conditions and films of the same thickness, the evolutions from one layer to another are generally well provided. The local structure of thin films was studied by μ-Raman scattering spectroscopy (LabRam HR800, Horiba Jobin-Yvon, NJ, USA) coupled with a ×100 microscope (Olympus, Japan) with the excitation wavelength of 785 nm. Thermal population effect at low wavenumbers was minimized by means of reduction of Raman intensity according Shuker and Gammon [22].

Two variable angle spectroscopic ellipsometers (J.A. Woollam Co., Inc., Lincoln, NE, USA) were employed in order to estimate the optical bandgap energy and refractive index dispersion of the fabricated films: first working in the UV-Vis-NIR range (300–2300 nm), the other in mid-IR (~300–6,000 cm^{-1}). The fundamental absorption edge was modelled by Cody-Lorentz oscillator model (described elsewhere [23]) to fit the ellipsometry data in the UV-Vis-NIR region. Within mid-IR range, the Sellmeier model was applied setting extinction coefficient to zero. The thickness of the films on borosilicate glass (Schott, BK7) was about 800 nm (±1 %) as determined by spectroscopic ellipsometry. Surface energy σ of thin films was determined following Owens-Wendt theory. Contact angles were obtained by computer controlled KSV CAM 100 USB video camera (KSV Instruments Ltd., Finland) at resolution of 640 × 480 px from curve fitting based on Young-Laplace equation of the sessile drop shape. Sessile drops of five standard liquids were recorded for 30 seconds immediately after the placing them onto the thin films surface. Equilibrium contact angle θ_{eq} was considered to be established after 30 seconds. All the contact angle measurements were carried out at 20 °C and ~30 % of relative humidity. Thin films used for the contact angle measurements were deposited at the electrical power of 10 W and the Ar pressure of 5×10^{-3} mbar onto 2-inch silicon wafers. The thickness of these films specifically deposited for contact angle measurements was in the range of ~600–700 nm. Contact angle was measured on the virgin thin films stored for a short time in the light isolated desiccator in order to ensure good reproducibility of the contact angle measurements.

3. Results and Discussion

3.1 Glass target characterisation

The average chemical composition of the targets is in good agreement with theoretical compositions. The DSC measurements performed with GSST glass targets have shown that the glass transition temperature T_g was decreasing with an increasing tellurium content from the initial value of 265 °C for tellurium-free composition of $Ge_{19}Sb_{17}Se_{64}$. Obtained values of T_g for $Ge_{19}Sb_{17}Se_{64-x}Te_x$ with $x = 5$, 10 and 15 were 247, 232 and 222 °C respectively (±2 °C). The T_g variation of about 40 °C with a substitution is observed for almost one quarter of selenium by tellurium. These results agree with the gradual introduction of tellurium atoms in substitution for selenium atoms, the binding energies of the vitreous network decreasing compared to those formed with selenium. This substitution could also have an effect on the crosslinking of the network, but probably to a lesser extent. The change in the difference between the T_g and the crystallization onset temperature T_x, one of the possible parameters showing the thermal stability of amorphous/glassy material, is also noticeable varying from T_x-$T_g \geq 150$°C to T_x-$T_g \sim 90$ °C with $x = 0$ to 15. For the last target with the highest proportion of tellurium, the distinction between its glass transition temperature and crystallization onset temperature is no longer clearly discernible, probably resulting in the formation of a glass-ceramic target. It should be noted that these large diameter bulk targets have very altered conditions of rapid cooling compared to the synthesis of glass of smaller dimensions, which exacerbates the possible formation of crystalline phases.

XRD analysis showed that obtained targets were vitreous with one exception. The diffraction peaks in the XRD patterns corresponding to $GeSe_2$ and $Sb_2Se_xTe_y$ (with $x + y = 3$, $x = 1$ or 2 and $y = 1$ or 2) phases appeared for target with nominal composition of $Ge_{19}Sb_{17}Se_{44}Te_{20}$ as shown in Fig. 1. Since the average composition of the partially crystalline target remains unchanged from the theoretical composition, the nature of the $Ge_{19}Sb_{17}Se_{44}Te_{20}$ glass-ceramic target should marginally influence the composition of the final thin film and its deposition rate, which nevertheless needs to be verified. The very fast quenching speeds during the sputtering process of GSST films on a silicon substrate at room temperature should make it possible to obtain amorphous films even if one of the targets is partially crystallized. The insert in Fig. 1 showing the XRD patterns of four GSST thin films deposited from the individual GSST targets under the same deposition conditions (15 W, Ar pressure of 5×10^{-3} mbar) fully confirms assumption described above.

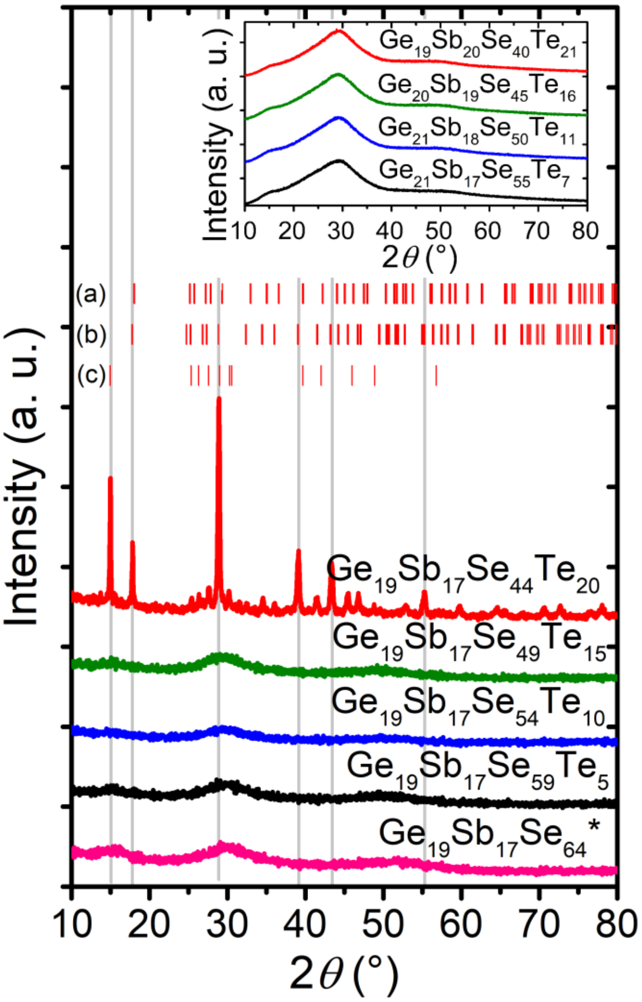

Figure 1. XRD patterns of bulk GSST target material with indicated powder diffraction patterns from crystallographic databases of Sb_2Se_2Te (a, COD ID 1008844), Sb_2SeTe_2 (b, COD ID 9007591), and $GeSe_2$ (c, ICDD 00-042-1104); Insert with XRD patterns of four thin films deposited from individual targets (four compositions) at same conditions – 15 W, Ar pressure of 5×10^{-3} mbar.

3.2 Chemical composition

All the depositions together with indicated electrical power, Ar working pressure and composition determined by EDS are summarized in Table 1. EDS results indicate that some minor differences in composition may take part when the Ar working pressure increases from 5×10^{-3} mbar to 1×10^{-2} mbar. With respect to the target composition, it can be seen that the composition of the deposited films tends in general to be close to the nominal values of the target while experiencing an increase of Ge from 1 to 3%, relatively stable values (~ +1–2%) for antimony and tellurium, and a rather more significant decrease for selenium of about 3–4%. Of course, these general trends will evolve more or less marginally with the variation of the composition and deposition parameters, which are for the latter relatively little adjustable in this work.

Looking in more detail at the composition change of the targets, very similar trends can be noted for the first three target compositions with an average value of 21% for Ge and 18% Sb with related deviation of 1.1% and 0.6%, respectively and for which globally the Se deficit (of about −4%) and the small Te excess (+1–2%) is respected from one target to another. A different behaviour is observed for the fourth, most Te-rich target, where a higher proportion of Sb (excess of +3%) compared to the target and lower concentration of Ge (19% on average, 1% deviation) compared with the other Se-richest films is consistently observed. This may be related to a somewhat enriched antimony concentration of the target itself for this (more difficult to fabricate) composition, but it would still appear that the increasing substitution of Te along the target compositions leads to a gradual increase in the proportion of antimony in the sputtered thin film.

Table 1. Deposition parameters: sputtering targets nominal chemical composition (at. %), electrical power applied on the cathode (W) and Ar pressure in the deposition chamber (× 10^{-3} mbar). Properties of the deposited thin films: deposition rate (nm.min^{-1}) chemical composition determined by EDS (±1 at. %), linear refractive index n_0 at 1.55 and at 7.7 µm (both ±0.01), and optical bandgap energy in eV determined by Cody-Lorentz oscillator model (E_g^{CL}, ±0.02 eV) from spectroscopic ellipsometry data analysis.

Theoretical target composition (at. %)	Power (W)	Ar pressure (× 10^{-3} mbar)	Deposition rate (nm · min^{-1})	Thin film composition (at. %)	Linear refractive index n_0		E_g^{CL} (eV)
					at 1.55 µm	at 7.70 µm	
$Ge_{19}Sb_{17}Se_{59}Te_5$	10	5	9.9	$Ge_{22}Sb_{17}Se_{55}Te_6$	2.91	2.84	1.33
	10	10	10.4	$Ge_{20}Sb_{17}Se_{56}Te_7$	2.84	2.78	1.37
	15	5	19.8	$Ge_{21}Sb_{17}Se_{55}Te_7$	2.87	2.81	1.37
	15	10	20.0	$Ge_{19}Sb_{17}Se_{56}Te_8$	2.84	2.78	1.41
$Ge_{19}Sb_{17}Se_{54}Te_{10}$	10	5	10.2	$Ge_{22}Sb_{18}Se_{50}Te_{10}$	2.97	2.89	1.27
	10	10	9.9	$Ge_{20}Sb_{17}Se_{51}Te_{12}$	2.91	2.83	1.33
	15	5	21.0	$Ge_{21}Sb_{18}Se_{50}Te_{11}$	2.96	2.88	1.25
	15	10	20.1	$Ge_{20}Sb_{18}Se_{51}Te_{11}$	2.91	2.84	1.27
$Ge_{19}Sb_{17}Se_{49}Te_{15}$	10	5	10.0	$Ge_{22}Sb_{18}Se_{45}Te_{15}$	3.07	2.98	1.11
	10	10	10.1	$Ge_{20}Sb_{18}Se_{46}Te_{16}$	3.00	2.92	1.18
	15	5	20.4	$Ge_{20}Sb_{19}Se_{45}Te_{16}$	3.05	2.96	1.20
	15	10	20.7	$Ge_{19}Sb_{18}Se_{46}Te_{17}$	3.02	2.93	1.21
$Ge_{19}Sb_{17}Se_{44}Te_{20}$	10	5	16.0	$Ge_{20}Sb_{20}Se_{40}Te_{20}$	3.20	3.09	1.05
	10	10	15.6	$Ge_{18}Sb_{20}Se_{40}Te_{22}$	3.17	3.06	1.12
	15	5	28.3	$Ge_{19}Sb_{20}Se_{40}Te_{21}$	3.18	3.07	1.05
	15	10	28.4	$Ge_{18}Sb_{20}Se_{40}Te_{22}$	3.14	3.04	1.08

The increase of Ar pressure slightly increases the amount of chalcogen elements, and thus the amount of heteropolar bonds in the films obtained when the Ar pressure increases from 5 × 10^{-3} to 1 × 10^{-2} mbar whatever the composition of the target and the applied power. An increased electrical power from 10 to 15 W at the same Ar pressure seems to increase the amount of heteropolar to a smaller extent [24]. It has been shown in the literature for two Ge-Sb-Se targets with different ratio of Ge/Sb ($R_{Ge/Sb}$ = 0.5 and 4.5) that increasing the Ar pressure increases the content of selenium and decrease the germanium concentration, while the electrical power has a minor effect but can affect the antimony concentration in the case of a high Ge/Sb ratio [24, 25]. For the GSST targets ($R_{Ge/Sb}$ = 1.2) with substitution of Se by Te, increasing Ar pressure or electrical power seems to increase the number of tellurium atoms (by 1% up to 2%) while the selenium content remains almost the same, perhaps slightly increased (+1%) but only with the effect of pressure and for the first three most selenium rich targets. The concentration of germanium and antimony has an expected behaviour considering the Ge/Sb ratio of these targets, [Sb] is indeed almost unaffected by Ar pressure and electric power while [Ge] tends to decrease slightly by 1–2% with Ar pressure and with electric power to a lesser extent more surprisingly. Therefore, for a given [Se/Te] ratio of the target, small compositional variation due to the change in pressure and electrical power could be responsible for minor changes in structure or optical properties.

3.2 Topography

AFM scans of 1 × 1 μm^2 area of sputtered films having a thickness of 800 nm, represented by figure 2A-D, have shown that the root mean square (RMS) roughness (Sq) of thin films surface increases with an increased tellurium content. Quantitatively, values of Sq increase from ~0.3±0.1 for $Ge_{19}Sb_{17}Se_{59}Te_5$ (fig. 2A) up to ~0.9±0.1nm for $Ge_{19}Sb_{17}Se_{44}Te_{20}$ (fig. 2D). This is clearly caused by the presence of large grains for films with tellurium content above 15 at. %.

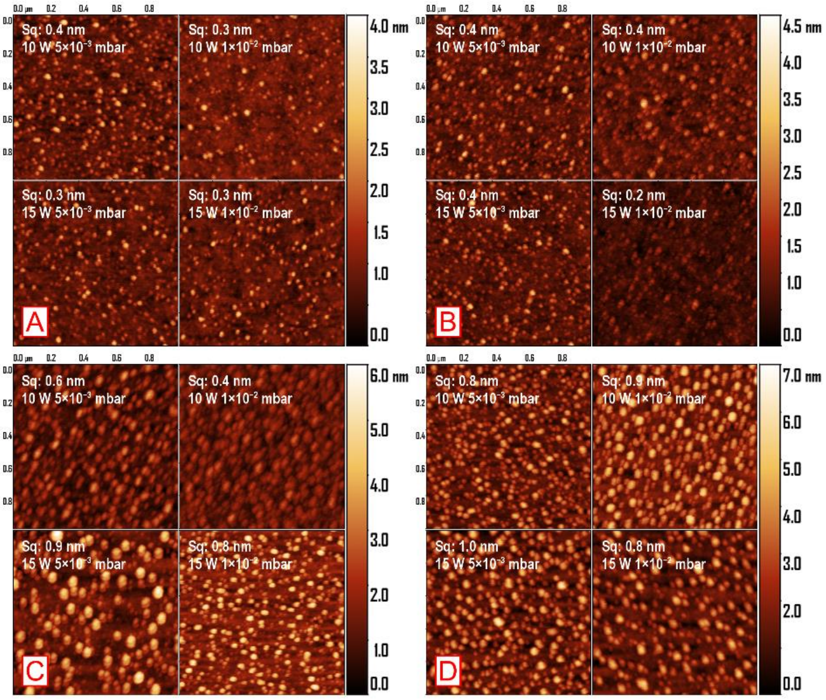

Figure 2. AFM scans of 1 × 1 μm^2 area of sputtered GSST thin films (with thickness of 800 nm) with indicated RMS roughness (Sq, ±0.1 nm), values on z-axis are normalized for each target nominal composition; A – $Ge_{19}Sb_{17}Se_{59}Te_{5.0}$, B – $Ge_{19}Sb_{17}Se_{54}Te_{10}$, C – $Ge_{19}Sb_{17}Se_{49}Te_{15}$, D – $Ge_{19}Sb_{17}Se_{44}Te_{20}$.

The work of Baudet *et al.* [25] studying the effect of decisive parameters of the sputtering process on the various properties of thin films in ternary Ge-Sb-Se system devoted to mid-IR sensor development, reports a significant variation of the roughness from 0.2 to 1 nm with a pressure varying from 5×10^{-3} to 1×10^{-2} mbar for the target composition richest in germanium considering an electric power lower than 17 W and a film thickness lower than 1 μm. The composition richer in antimony is more stable in terms of roughness with Ar pressure variation. The addition of a few percent of tellurium to $Ge_{19}Sb_{17}Se_{64}$ composition seems to make the roughness of the films relatively insensitive to the change of Ar pressure and to a lesser extent to the change in electrical power. To conclude, the roughness is essentially governed by the percentage of tellurium and could have a detrimental effect on the final optical losses of the photonics system used as a transducer for the IR medium optical sensor. It is therefore important, when selecting the ideal composition of the IR sensor's guiding layer, to make a compromise with the increasing introduction of tellurium between the gradual increase in roughness and the expected increase in both the increase in transmission in the IR domain and the refractive index in order to increase the index contrast and, consequently, the confinement of IR light.

3.3 Optical properties

Linear refractive index and optical band-gap energy. The effect of the [Te/Se] target composition ratio and deposition conditions on the optical properties, specifically linear refractive index (n_0) and optical bandgap energy (E_g^{CL}), were studied by spectroscopic ellipsometry. These results are summarized in the Table 1. Moreover, the dispersion curves are shown in Figure 3A–D. As seen, the substitution of selenium by heavier tellurium atoms, having higher polarizability, increases the linear refractive index.

At the same time, the optical bandgap energy decreases as expected in accordance with semi-empirical Moss rule [26]. For the clarity, the dependencies of linear refractive index at 1.55 and 7.7 µm, as well as the optical bandgap energy on the tellurium content are depicted in Figure 4. Values of refractive index at 7.7 µm allow the evaluation of potential suitability of fabricated thin films for mid-infrared sensor application. Baudet *et al.* successfully applied chalcogenide thin films with composition $Ge_{12.5}Sb_{25}Se_{62.5}$ as a waveguide guiding layer for the evanescent wave sensor for the detection of pollutants in water. The refractive index n_0 at 7.7 µm of these sputtered thin films is 2.77 (±0.01) and the refractive index contrast with the cladding layer is about $\Delta = 0.33$ at 7.7 µm for an Ar pressure of 1×10^{-1} mbar during the sputtered films deposition [15]. Among all used targets, the one with the composition $Ge_{19}Sb_{17}Se_{59}Te_5$ seems to be suitable as a potential replacement of Te-free GSS target for the guiding layer. Thin film with composition $Ge_{21}Sb_{17}Se_{55}Te_7$, having values of n_0 at 7.7 µm and bandgap energy E_g^{CL} of 2.81 (±0.01) and 1.37 eV (±0.02) can potentially be used as a guiding layer for the evanescent wave sensors mentioned above [6]. Indeed, the refractive index contrast at 7.7 µm between this thin film and a cladding layer with composition of $Ge_{28.1}Sb_{6.3}Se_{65.6}$ used in such sensors would be 0.32 for the deposition parameters considered in this study (Table 1). Considering the deposition parameters, it can be noted that the linear refractive index decreases with an increasing argon pressure. Similar changes were observed by Baudet *et al.* in ternary Ge-Sb-Se thin films justified by changes in morphology and/or porosity as well as the roughness of sputtered films related to important variation of pressure between 5×10^{-3} to 5×10^{-2} mbar [25]. The effect of the later was not proven in quaternary Ge-Sb-Se-Te as the AFM topography shows only small divergence when argon pressure was increased between 5×10^{-3} to 1×10^{-2} mbar only. The decrease of linear refractive index and the increase of E_g^{CL} with an increased pressure of argon in the variation range used for this study may be justified by other contributions and would be more related to the changes in composition of the GSST thin film reflected by R variation.

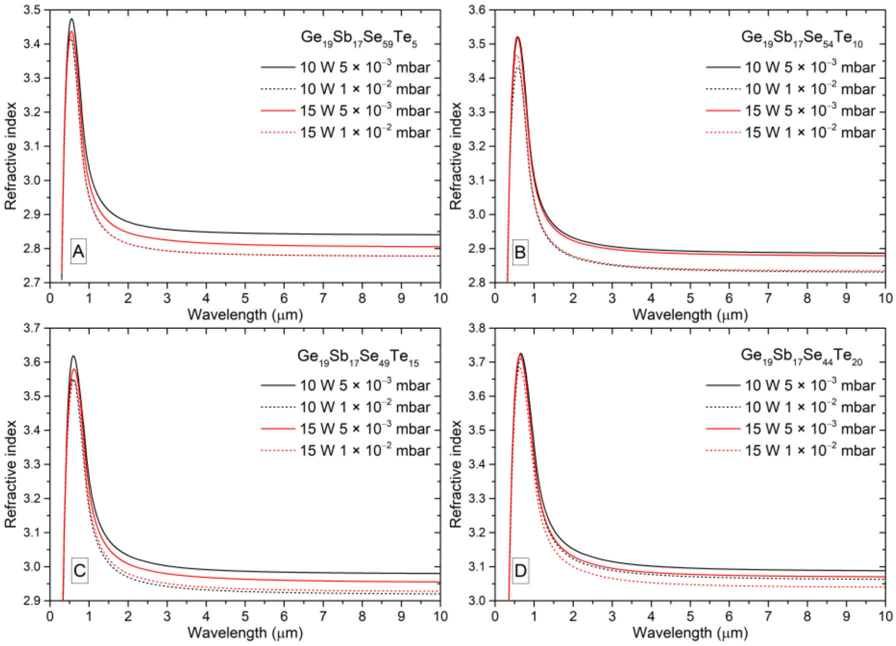

Figure 3. Spectral dependencies of linear refractive indices of sputtered GSST thin films with indicated nominal compositions of the GSST target and deposition conditions.

As already mentioned, the increase in Ar pressure results in higher proportions of chalcogen atoms (Se and Te) compared to metalloids (Ge, Sb) favouring the heteropolar bond formation. This leads to changes in n_0 and E_g^{CL} as depicted in Figure 4. The electrical power change from 10 to 15 W seem to have less significant effect on optical properties. As follows from the above mentioned, the effect of the minor changes in compositions seem to have rather low effect on the fundamental absorption edge and thus reflects only small changes in the localized/tail states.

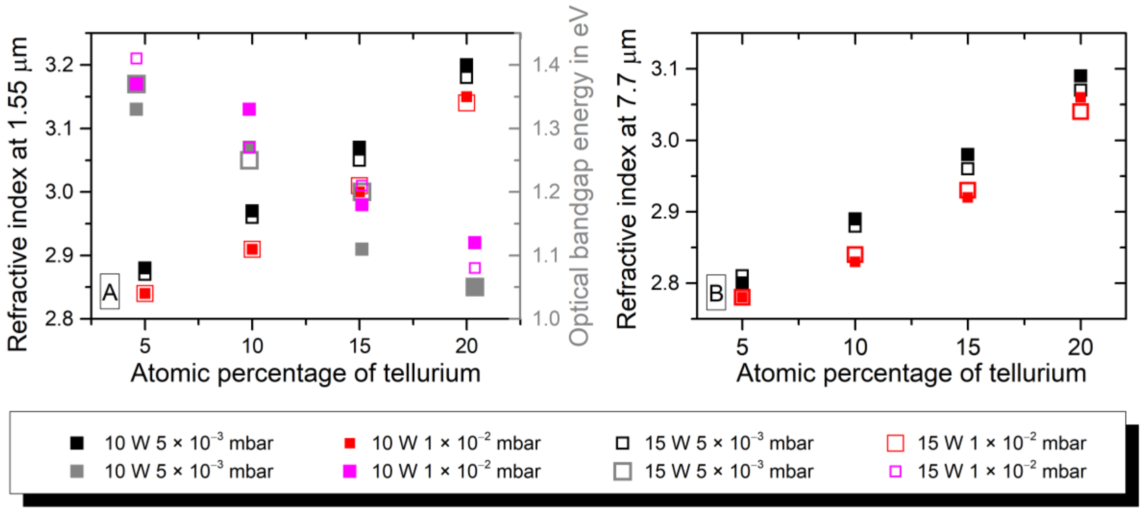

Figure 4. A – Dependence of linear refractive index at 1.55 µm and the optical bandgap energy E_g^{CL} on tellurium content, B – Dependence of linear refractive index at 7.7 µm on tellurium content.

NLO properties of GSST films. The objective of nonlinear material selection for NLO devices should be to lead to a negligible linear absorption α, the largest value of nonlinear refractive index (n_2) and the smallest value of two photon absorption (TPA), defined by nonlinear absorption coefficient β, to optimize the nonlinear figure of merit ($FOM = \frac{n_2}{\lambda\beta}$). According to classical modelling used to predict the nonlinear coefficients, like Sheik-Bahae method [27], the bandgap energy of amorphous chalcogenide thin films must be at least higher than ~1.6 eV to obtain a negligible TPA at the 1.55 µm telecommunication wavelength. In selenide or seleno-telluride thin films, one can possibly consider for smaller E_g to be able to keep an interesting *FOM* if the n_2 growth is faster than the TPA increase. The calculated values of nonlinear refractive index at telecommunication wavelength of 1.55 µm and at 7.7 µm mid-IR wavelength using Sheik-Bahae's formalism are plotted in Figure 4A5A. Qualitatively, values of n_2 at 1.55 µm decrease with increasing value of linear refractive index n_0 while the opposite is true for n_2 at 7.7 µm. This is due to the shape of the dispersion function for n_2 within the used model, which becomes negative for approximately $\hbar\omega \geq 0.7E_g$ when photon energy approaches resonance energy [28, 29]. Consequently, the negative values of n_2 at 1.55 µm were found for films $Ge_{20}Sb_{20}Se_{40}Te_{20}$ (E_g^{CL} = 1.05 eV, n_0 = 3.20), $Ge_{19}Sb_{20}Se_{40}Te_{21}$ (E_g^{CL} = 1.05 eV, n_0 = 3.18) and $Ge_{18}Sb_{20}Se_{40}Te_{22}$ (E_g^{CL} = 1.08 eV, n_0 = 3.14). Similar observation was reported for some chalcogen poor and high Te concentration GSST by Dory *et al.* [28].

The maximum value of n_2 at 1.55 µm, specifically 28×10^{-18} m$^2 \cdot$ W^{-1}, was found for thin film with composition $Ge_{20}Sb_{17}Se_{56}Te_7$ (E_g^{CL} = 1.37 eV, n_0 = 2.84, $\beta = 2.2 \times 10^{-10}$ m · W^{-1}, *FOM* = 0.08). Moreover, thin film with composition $Ge_{19}Sb_{17}Se_{56}Te_8$ (E_g^{CL} = 1.41 eV, n_0 = 2.84, $\beta = 1.6 \times 10^{-10}$ m · W^{-1}), having the same value of n_2 shows the highest *FOM* at 1.55 µm among all fabricated GSST films (*i.e.* 0.11).

Overall, calculated values of nonlinear refractive index of deposited GSST films, ranging from 16 to 28 m$^2 \cdot$ W^{-1} (excluding negative values), are higher than reported calculated values of n_2 for GSS thin films which are in the range from 5 to 23 m$^2 \cdot$ W^{-1} but the two photon absorption (TPA) coefficient (β) is also expected to be higher [28]. Values of β at 1.55 µm for GSST are within the range of ~2–6 × 10^{-10} m · W^{-1} leading to *FOM* of ~0.01–0.11 (excluding negative values due to negative n_2). It should be noted that values of β in tellurium-free GSS having E_g^{CL}>1.60 eV are typically ~0.1 × 10^{-10} m · W^{-1} [30]. Nonlinear optical properties of GSST thin films studied in this work compared to available references are summarized in table 2.

Table 2. Comparison of nonlinear optical properties of GSST thin films with various references and with As_2Se_3 bulk glass; chemical composition of thin films (±1 at. %), linear refractive index n_0 at 1.55 μm (±0.01), optical bandgap energy in eV (E_g^{CL}, ±0.02 eV), nonlinear refractive index n_2 (× 10^{-18} m^2 · W^{-1}), TPA coefficient β (× 10^{-10} m · W^{-1}) and *FOM* at 1.55 μm.

Composition (at. %)	n_0 at 1.55μm	E_g^{CL} (eV)	n_2 at 1.55 μm (× 10^{-18} m^2 · W^{-1})	β at 1.55 μm (× 10^{-10} m · W^{-1})	*FOM* at 1.55 μm	Reference
$Ge_{19}Sb_{17}Se_{56}Te_8$	2.84	1.41	28	2	0.11	this work
$Ge_{20}Sb_{17}Se_{51}Te_{12}$	2.91	1.33	26	3	0.06	this work
$Ge_{19}Sb_{18}Se_{46}Te_{17}$	3.01	1.21	17	4	0.03	this work
$Ge_{18}Sb_{20}Se_{40}Te_{22}$	3.17	1.12	6	5	0.01	this work
$Ge_{19}Sb_{17}Se_{64}$	2.68	1.86	8±2	0.37±0.05	0.14	[14]
$Ge_{16}Sb_{20}Se_{64}$	2.69	1.68	9	N/A	0.56[1]	[30]
$Ge_{23}Sb_{16}Se_{61}$	2.67	1.65	11	N/A	0.73[1]	[30]
$Ge_{28}Sb_{12}Se_{60}$	2.66	1.66	11	N/A	0.70[1]	[30]
$Ge_9Sb_{20}Se_{71}$	2.76	1.68	10	N/A	0.65[1]	[30]
$Ge_{12}Sb_{25}Se_{63}$	2.80	1.65	11	N/A	0.73[1]	[30]
$Ge_7Sb_{25}Se_{68}$	2.86	1.61	13	N/A	0.86[1]	[30]
$Ge_{28}Sb_{15}Se_{52}Te_5$	2.94	1.29	36	N/A	N/A	[28]
$Ge_{40}Se_{39}Te_{21}$	2.92	1.26	44	N/A	N/A	[28]
$Ge_{27}Sb_{25}S_{48}$	2.79	1.34	25	N/A	N/A	[28]
$As_{40}Se_{60}$	2.80	1.70	9	N/A	0.58[1]	[30]
$As_{40}Se_{60}$ glass	2.78–2.84	1.74[2]	12–13	0.25	~2	[31-33]

[1] Calculated according Sheik-Bahae with $\beta = 0.1 \times 10^{-10}$ m · W^{-1}

[2] Tauc gap

It should be mentioned that the calculated values of n_2 and β in the present work are only order of magnitude estimations as the Sheik-Bahae's formalism is intended for the determination of Kerr coefficient and the two-photon absorption coefficient of direct-gap semiconductors. It should be kept in mind that amorphous chalcogenides are considered as non-direct gap materials and in this model, the tail and localised states related to amorphous materials are not taken into account, which is also the case for the Dinu model [34]. Moreover, the presence of uncertainties in the physical parameters used in the Sheik-Bahae's formalism enlarge the error in the estimation. It should be noted that calculated values of n_2 obtained in this work are generally somewhat lower relative to those reported by Dory *et al.* [28]. In spite of this, used formalism allows to have a fairly good predictive vision on the n_2 and β of amorphous chalcogenides by considering their refractive index and optical band-gap indicating trends that were verified experimentally for Ge-Sb-Se bulk glasses or thin films for which an error of experimental measurement of the order of ±10-20% is expected [12, 30, 31, 33]. For instance, Olivier *et al.* reported experimental values of nonlinear refractive index (n_2) at 1.55 μm for bulk sample of $Ge_{19.4}Sb_{16.7}Se_{63.9}$ glass around 10±2.0 × 10^{-18} m^2 · W^{-1} and β around 0.31 cm · GW^{-1} obtained by direct transmission analysis [12]. Moreover, Kuriakose *et al.* reported experimental values at 1.55 μm of 8±2 × 10^{-18} m^2 · W^{-1} (n_2) and β around 0.37±0.05 cm · GW^{-1} for chalcogenide slab waveguides of 3 μm thickness prepared from $Ge_{19.4}Sb_{16.7}Se_{63.9}$ target using beam self-trapping analysis [14]. Besides that, values of nonlinear refractive index calculated for GSST films are higher than those obtained for amorphous Ge-Sb-Se thin films with experimental values reaching the maximum value of n_2 at 1.55 μm about 21±3.0 × 10^{-18} m^2 · W^{-1} for amorphous $Ge_3Sb_{35}Se_{62}$ [30]. The highest nonlinearity at 7.7 μm by means of n_2 was found for thin film $Ge_{19}Sb_{20}Se_{40}Te_{21}$ (E_g^{CL} = 1.05 eV, n_0 = 3.18).

This is the consequence the strong TPA absorption at 1.55 μm in these films as depicted in Figure 5B. The trade-off between optical bandgap energy and the refractive index plays the crucial role when evaluating the nonlinear optical properties of materials. Lower optical bandgap energies of GSST relative to GSS thin films would indicate the possible limitation of these materials in terms of application in nonlinear optics at 1.55 μm due to the high multi-photon absorption such as TPA absorption. This results in relatively low values of figure of merit 1.55 μm as shown in Figure 5B.

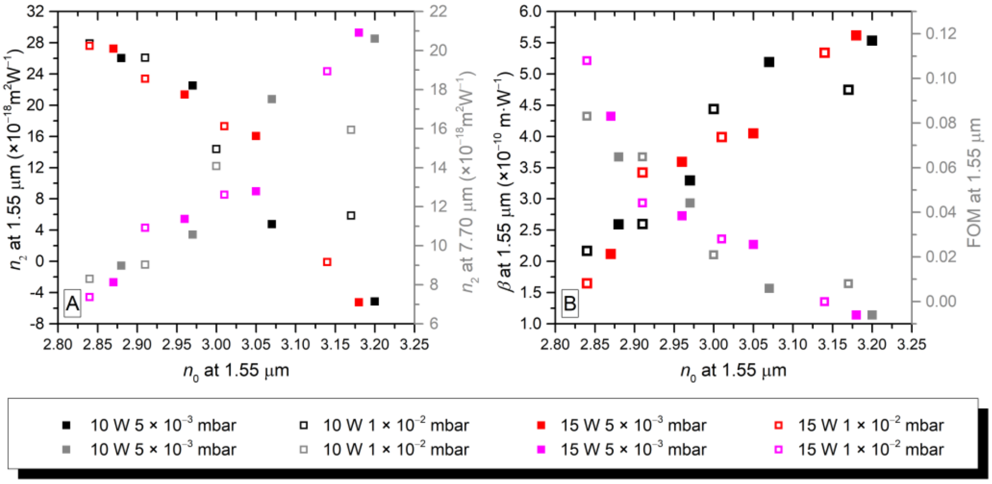

Figure 5. (A) Dependence of nonlinear refractive index n_2 on linear refractive index n_0 at 1.55 µm. (B) Dependence of TPA coefficient β and figure of merit *FOM* on linear refractive index n_0 at 1.55 µm.

3.4 Wettability

Surface energy σ of thin films plays an important role when considering the potential application of these materials for chemical sensors. It is important to have an idea of the intrinsic surface energy before any functionalization of the chalcogenide film surface and the possible influence related to the tellurium concentration. Obtained contact angles for five standard liquids are summarized in Table 3. These were used for the calculation of values of dispersive γ_S^d and polar γ_S^p components together with the total surface energy σ of the GSST thin films using Owens-Wendt theory (Figure 6) – γ_S^d is obtained as a square of an intercept value and γ_S^p square of a slope value of a linear fit respectively.

Table 3. Compositions of GSST sputtered films determined by EDS (±1 at. %), RMS roughness (Sq, ±0.1 nm) obtained from AFM scans, contact angles for standard liquids, dispersive γ_S^d and polar γ_S^p components of surface energy obtained by Owens-Wendt theory (both ±2 mN · m^{-1}) and the values of surface energy σ (±2 mJ · m^{-2}) of thin films.

Thin film composition (at. %)	*Sq* (nm)	Contact angle, θ (°)					γ_S^d (±2 mN·m⁻¹)	γ_S^p (±2 mN·m⁻¹)	σ (±2 mJ·m⁻²)
		Water	ethylene glycol	formamide	glycerol	diiodomethane			
$Ge_{22}Sb_{17}Se_{55}Te_6$	0.4	70±3	59±1	61±1	69±1	41±1	29	7	37
$Ge_{22}Sb_{18}Se_{50}Te_{10}$	0.4	71±1	56±1	61±1	67±1	42±1	30	7	39
$Ge_{22}Sb_{18}Se_{45}Te_{15}$	0.6	68±2	54±2	61±2	66±2	39±1	31	8	38
$Ge_{20}Sb_{20}Se_{40}Te_{20}$	0.8	54±2	47±1	51±1	75±1	54±2	22	17	39

As seen from Table 3, the values of surface energy for all the four compositions lie between ~37–39 mJ · m^{-2}. These values are lower than those obtained by Baudet *et al.* for tellurium-free GSS thin films with the composition of $Ge_{28.1}Sb_{6.3}Se_{65.6}$ and $Ge_{12.5}Sb_{25}Se_{62.5}$ respectively. They obtained the values of about 46 mJ · m^{-2} for both compositions with negligible polar components (~1 mN · m^{-1}) [10]. Moreover, Lucas *et al.* studied the contact angles of different liquids on polished bulk discs of $Te_{20}As_{30}Se_{50}$ glass for which the surface roughness is expected to be higher than chalcogenide thin films [35]. Quantitatively, they obtained the contact angles of 73±3° and 62±3° for water and glycerol respectively. The surface roughness rise usually increases the wettability as observed for these bulk chalcogenide glasses. In case of sputtered GSST films, the wettability just slightly increased when the tellurium content increases from 5 to 15 at. % for most of the used liquids. However, for the thin film with the tellurium content of 20 at. %. the contact angle is enlarged for glycerol and diiodomethane while for the others it is decreased. This causes the decrease of the intercept of the linear fit justified by the important decrease of the dispersive component of surface energy of this film as depicted in Figure 6. In the same time, the small contact angle measured for the distilled water increases the slope of the linear fit enlarging the polar component of the surface energy of this film. The $Ge_{19}Sb_{17}Se_{44}Te_{20}$ thin film seems to present an increased polarity of the surface, which might be explained by higher surface oxidation related to presence of tellurium in higher content or influence of surface roughness.

Surface oxidation can be a problem encountered for bulk glass, preform, optical fibers and thin films or waveguides based on chalcogenides. In order to prevent them from oxidation, many strategies are applied such as surface purification, distillation, chemical and mechanical polishing, cladding, coating, surface passivation, etc. Protection against the influence of the atmosphere by a chemical barrier layer can be performed during the manufacture of chalcogenide waveguides in order to limit optical losses, in particular by the deposition of Al_2O_3, Si_3N_4 or SiO_2 on the surface if needed for photonics applications. However, it is first necessary to know well the chalcogenide material by taking care to characterize it before proceeding to the fabrication of the mentioned heterostructure to improve its performances. The nature of the specific surface of the thin films plays a preponderant role in this possible oxidation whatever the physical vapor deposition technique used [21, 25, 36].

In case of spectroscopic ellipsometry, the three-layer model is typically used consisting of substrate, film layer itself, and the surface layer/roughness. The thicknesses of surface layer were fitted as ~1.6, ~1.7, ~1.6 and ~2.2 nm. Inherently, surface layer/roughness evaluated by ellipsometry is larger than surface roughness obtained from AFM. The thickness values of the surface layer/roughness shown above appear to be comparable to those of the sulphide/selenide thin films, which could lead to the conclusion that the seleno-telluride thin films do not oxidize more than the sulphides/selenides. Moreover, at such small thickness this oxide layer should not contribute significantly to optical losses. Nevertheless, further studies to discriminate between these two factors, i.e. surface oxidation and surface roughness, and to avoid any correlation effect should be conducted in future.

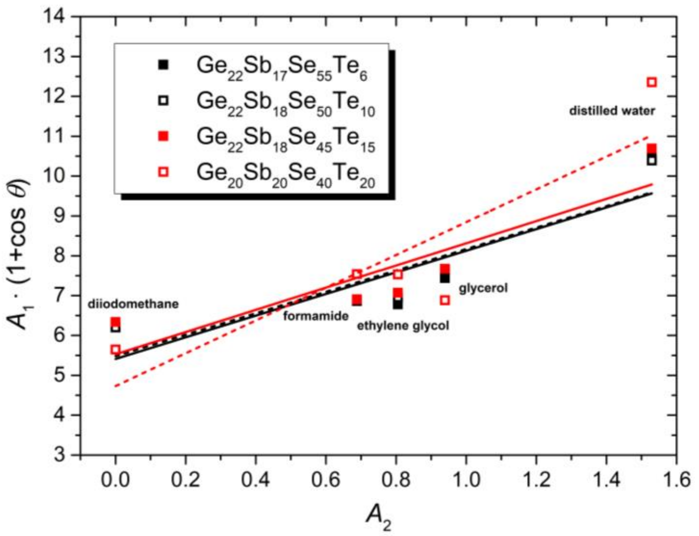

Figure 6. Owens−Wendt plot for GSST thin films on silicon wafer with indicated nominal composition (10 W, 0.5 Pa); $A_1 = \gamma_L / 2\sqrt{\gamma_L^d}$ and $A_2 = \sqrt{\frac{\gamma_L^p}{\gamma_L^d}}$, where γ_L^d and γ_L^p stands for the dispersive and polar component of the surface tension of the standard liquid γ_L, respectively.

3.5 Local structure

The influence of the increasing tellurium content on the structure of thin films deposited at 10 W and Ar working pressure of 5×10^{-3} mbar is represented by the Raman scattering spectra shown in Figure 7-A. For comparison, the spectra of sputtered thin film from Te-free $Ge_{19}Sb_{17}Se_{64}$ target deposited at 15 W at the same Ar working pressure is also shown.

For films sputtered from $Ge_{19}Sb_{17}Se_{59}Te_5$ target, the Raman spectra are *prima facie* dominated by two contributions, the main peak at ~160 cm^{-1} with an adjacent asymmetric shoulder with the maxima at ~197 cm^{-1}. The two peaks shift gradually towards the lower wavenumbers with an increasing tellurium content in GSST thin films. As a result, the former is peaking at ~153 cm^{-1}, the later at ~194 cm^{-1} in $Ge_{19}Sb_{17}Se_{44}Te_{20}$. The adjacent asymmetric shoulder (from 197 to 194 cm^{-1}) seems to find its origin in the symmetric stretching vibrations of Ge–Se bonds, typically at ~198 and ~216 cm^{-1}, in corner-sharing and edge-sharing [$GeSe_4$] tetrahedra, respectively.

In the Raman spectra of Te-free $Ge_{19}Sb_{17}Se_{64}$ thin film, this peak (~200 cm^{-1}) and its shoulder (~214 cm^{-1}) are better observed. For this pure selenide film, they are mainly accompanied by an additional shoulder (at ~175 cm^{-1}) related to Ge-Ge stretching modes in [$GeSe_{4-y}Ge_y$] distorted tetrahedra with y = 1,2,3 and ethane-like $Se_3Ge–GeSe_3$. They are also complemented by an important contribution (at ~190 cm^{-1}) of Sb-Se stretching mode of [$SbSe_3$] pyramids and probably vibration modes related to Ge-Sb bonds around 165 cm^{-1} [12, 24]. and finally by a small broad band observed between 250–315 cm^{-1} with several contributions mainly from (Se-Se) stretching mode from ~245 cm^{-1} to ~265 cm^{-1} coming from –(Se–Se)n– long chains to –(Se–Se)– dimers and also ν_{as} [$GeSe_4$] [37] (Figure 7-A).

In the case of the GSST thin films, these different bands and shoulders related to [$GeSe_4$], Ge–Ge and Se–Se vibration modes seem to disappear gradually with the [Te] increase to the profit of the main band at lower frequency. In the structure of multicomponent glasses and thin films which contain more than one chalcogen element, mixed entities such as [$GeSe_{4-x}Te_x$] and [$SbSe_{3-x}Te_x$] can be at the origin of the main broad peak observed at ~160 cm^{-1} as referred by Abdellaoui *et al.* in quinary $Ga_5Ge_{20}Sb_{10}Se_{65-x}Te_x$ (x=10–37.5 at. %) bulk glasses [38] and by Gonçalves *et al.* for ternary $Ge_{20}Te_{80-x}Se_x$ bulk glass [37]. The broad band can have also non negligible contributions related to the presence of Ge(Sb)–Ge(Sb) bonds because the GSST films present a deficit in selenium as observed for Te-free $Ge_{19}Sb_{17}Se_{64}$ with vibration modes localised from 150 (mainly related to vibration modes of (Sb-Sb) bond in $SbSe_2–SbSe_2$ entities) to 175 cm^{-1} [12, 24, 39].

Even if the GSST films present a deficit of selenium, the presence of Se–Te and even Te–Te can be envisaged, as Se-Se bonds are present in small proportion in $Ge_{19}Sb_{17}Se_{64}$ thin film. It can be noted that vibration modes of (Te–Te) bond from $–(Te–Te)_n–$ chains to dimer possess vibrations modes in the range from 145 to 165 cm^{-1} [40] and might slightly contribute to the main broad bands centred at 160 cm^{-1} while vibration modes of (Te–Se) bonds inside mixed chains or mixed dimers could present vibration modes in the range of 208–266 cm^{-1} [37, 41]. It was proposed in the case of $Ge_{20}Te_{80-x}Se_x$ chalcogen rich glass that the substitution of Te to Se in small proportion will lead to the introduction of Te inside the $–(Se–Se)_n–$ chains before to bond [$GeSe_4$] tetrahedra forming finally mixed entities when the tellurium increases. It could be also the case in the GSST films but it is important to keep in mind that the chemical composition of the $Ge_{19}Sb_{17}Se_{64-x}Te_x$ targets is stoichiometric and the GSST films present a deficit of selenium compare to the targets. Apart from bonding defects generated by a statistical disorder inherent to amorphous chalcogenides, the selenium deficit limits the chalcogen-chalcogen bonds occurrence while it substantially should increase the proportion of Ge(Sb)–Ge(Sb) bonds. All these mixed entities and homopolar bond modifications will have an important impact on the electronic band structure and localized/tail states of amorphous GSST thin films and on the hyperpolarizability of the entities and bonds present in the amorphous lattice substantially modifying their bandgap E_g and nonlinear properties.

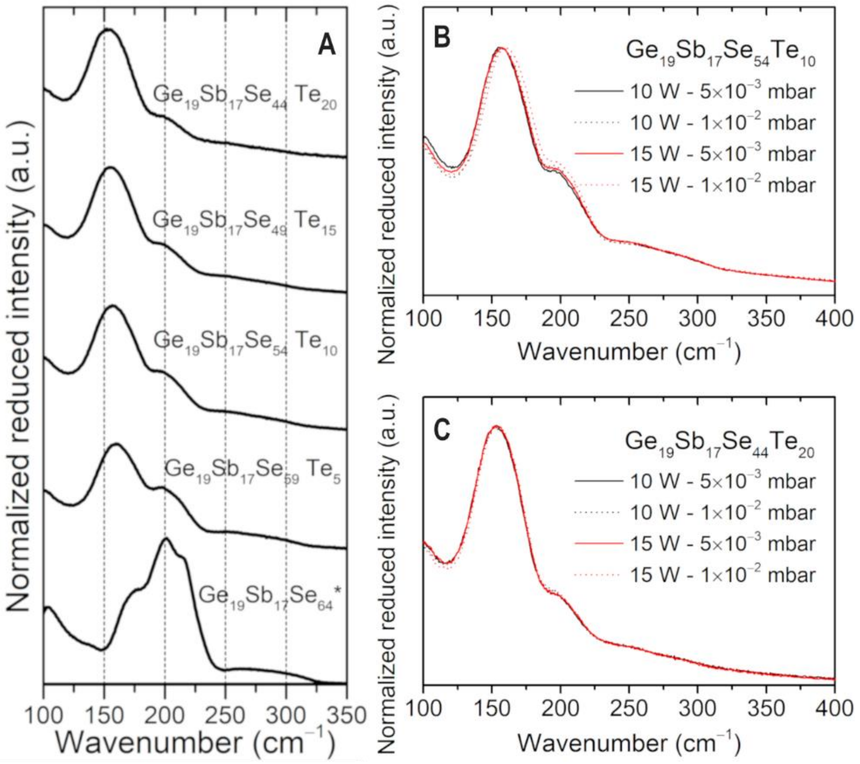

Figure 7. Raman spectra of sputtered GSST thin films : A – indicated theoretical target compositions (* from [13]), and deposition conditions : B – Target $Ge_{19}Sb_{17}Se_{54}Te_{10}$, C – Target $Ge_{19}Sb_{17}Se_{54}Te_{10}$

Moreover, the Raman spectra of GSST films are strongly affected when tellurium is introduced even in small proportion, as it was also observed in stoichiometric $Ga_5Ge_{20}Sb_{10}Se_{65-x}Te_x$ glasses much more rapidly than in the case of a system rich in chalcogen [37, 41]. Thus, the shift of the main broad band from 160 cm^{-1} to 153 cm^{-1} can be mainly explained by the increase of the substitution of Se by Te in the mixed entities as [$GeTe_4$] present a stretching vibration mode centered at 130 cm^{-1} [37, 40, 42] and [$SbTe_3$] pyramidal units or defective octahedral present Raman active band at 145 cm^{-1} [43].

The changes of deposition conditions by means of the increased electrical power and/or argon pressure do not seem to affect the local structure significantly and less and less with tellurium content increase. The pressure and electrical power increase have an effect on ν_s[$GeSe_4$] intensity with a slight increase and on the position of the main band at 160 cm^{-1} slightly shifted to higher wavenumber.

4. Conclusions

GSST thin films were fabricated by rf magnetron sputtering from glass-ceramics targets with nominal composition of $Ge_{19.4}Sb_{16.7}Se_{63.9-x}Te_x$ (x=5, 10, 15, 20). The structure of GSST amorphous films according to Raman analysis seems to be built mainly by selenide and mixed entities in variable proportion according to the tellurium concentration such as [$GeSe_{4-x}Te_x$] and [$SbSe_{3-x}Te_x$] (x = 0, 1, 2) and in all likelihood homopolar Ge(Sb)–Ge(Sb) bonds to compensate for the chalcogen deficiency. The contact angle measurements have shown values of 68-71° for water of the GSST thin films resulting in values of surface energy of about ~36–39 mJ · m^{-2}. The presence of 20 at. % of tellurium increases the polar component of the surface energy of the thin film and decrease the contact angle to 54° which might be related to the oxidation of the surface in link with the composition and also roughness increase. Analysis of ellipsometric data revealed the increase of linear refractive index with increasing tellurium concentration while the optical bandgap energy decreases. Moreover, the former seems to decrease with the increasing working pressure of argon from 5×10^{-3} to 1×10^{-2} mbar, which is mainly related to the composition changes. The electrical power change from 10 to 15 W seem to have insignificant effect. Among all used targets, the one with the composition $Ge_{19}Sb_{17}Se_{59}Te_5$ seems to be suitable as a potential replacement of Te-free GSS target for the guiding layer. Indeed, the refractive index contrast at 7.7 μm between a GSST thin film and a cladding layer with composition of $Ge_{28.1}Sb_{6.3}Se_{65.6}$ used in such sensors would be at least equal to 0.32. By adjusting the Te/Se composition, it is possible to control the index contrast between the guiding layer and the buffer layer in order to create an efficient IR sensor in terms of evanescent fields and with compact dimensions.

Furthermore, it was shown that thin film with composition $Ge_{19}Sb_{17}Se_{56}Te_8$, having nonlinear refractive index $n_2 \sim 28 \times 10^{-18}$ m$^2 \cdot$ W^{-1}, shows the highest *FOM* at 1.55 µm among all fabricated films. Calculated values of n_2 for GSST films are within the rage from 16 to 28 × 10^{-18} m$^2 \cdot$ W^{-1} (excluding negative values). The potential limitation of these materials when the concentration in tellurium increase may lie in low values of optical bandgap energies resulting in high two-photon absorption at telecommunication wavelength (*i.e.* 1.55 µm) which will not be the case for mid-IR. To conclude, wide IR transparency in combination with high (non)linear refractive indices make these materials suitable for potential applications in the field of mid-infrared devices such as optical switches and sensors.

5. Acknowledgements

Platform Spectroscopy Infrared and Raman (SIR – ScanMAT, Université de Rennes 1) and CMEBA are acknowledged for performed Raman and EDS measurements, respectively.

Funding: This work was supported by the CNRS, Brittany region (France), ANR LOUISE (ANR-15-CE04-0001-01), ANR AQUAE (ANR-21-CE04-0011) and Czech Science Foundation (Project No. 19-24516S).

References

[1] S.R. Ovshinsky, P.H. Klose, Amorphous and Liquid Semiconductors Imaging in amorphous materials by structural alteration, Journal of Non-Crystalline Solids 8 (1972) 892-898.
[2] J.A. Savage, S. Nielsen, Chalcogenide glasses transmitting in the infrared between 1 and 20 µ — a state of the art review, Infrared Physics 5(4) (1965) 195-204.
[3] K. Tanaka, Optical Nonlinearity in Photonic Glasses, in: S. Kasap, P. Capper (Eds.), Springer Handbook of Electronic and Photonic Materials, Springer International Publishing, Cham, 2017, pp. 1-1.
[4] M. Wuttig, N. Yamada, Phase-change materials for rewriteable data storage, Nature Materials 6(11) (2007) 824-832.
[5] J. Tang, F. Yuan, X. Shen, Z. Wang, M. Rao, Y. He, Y. Sun, X. Li, W. Zhang, Y. Li, B. Gao, H. Qian, G. Bi, S. Song, J.J. Yang, H. Wu, Bridging Biological and Artificial Neural Networks with Emerging Neuromorphic Devices: Fundamentals, Progress, and Challenges, Advanced Materials 31(49) (2019) 1902761.
[6] E. Baudet, A. Gutierrez-Arroyo, M. Baillieul, J. Charrier, P. Němec, L. Bodiou, J. Lemaitre, E. Rinnert, K. Michel, B. Bureau, J.L. Adam, V. Nazabal, Development of an evanescent optical integrated sensor in the mid-infrared for detection of pollution in groundwater or seawater, Advanced Device Materials 3(2) (2017) 23-29.
[7] H.P.T. Nguyen, T.H. Tuan, L. Xing, M. Matsumoto, G. Sakai, T. Suzuki, Y. Ohishi, Supercontinuum generation in a chalcogenide all-solid hybrid microstructured optical fiber, Opt. Express 28(12) (2020) 17539-17555.
[8] N. Sharma, S. Sharda, V. Sharma, P. Sharma, Far-infrared investigation of ternary Ge–Se–Sb and quaternary Ge–Se–Sb–Te chalcogenide glasses, Journal of Non-Crystalline Solids 375 (2013) 114-118.
[9] A. Ganjoo, H. Jain, S. Khalid, C.G. Pantano, Structural modification of Ge–Se amorphous films with the addition of Sb, Philosophical Magazine Letters 85(10) (2005) 503-512.

[10] E. Baudet, A. Gutierrez-Arroyo, P. Němec, L. Bodiou, J. Lemaitre, O. De Sagazan, H. Lhermitte, E. Rinnert, K. Michel, B. Bureau, J. Charrier, V. Nazabal, Selenide sputtered films development for MIR environmental sensor, Opt. Mater. Express 6(8) (2016) 2616-2627.
[11] E. Delcourt, N. Jebali, L. Bodiou, M. Baillieul, E. Baudet, J. Lemaitre, V. Nazabal, Y. Dumeige, J. Charrier, Self-phase modulation and four-wave mixing in a chalcogenide ridge waveguide, Opt. Mater. Express 10(6) (2020) 1440-1450.
[12] M. Olivier, J.C. Tchahame, P. Němec, M. Chauvet, V. Besse, C. Cassagne, G. Boudebs, G. Renversez, R. Boidin, E. Baudet, V. Nazabal, Structure, nonlinear properties, and photosensitivity of (GeSe2)100-x(Sb2Se3)x glasses, Opt. Mater. Express 4(3) (2014) 525-540.
[13] M. Baillieul, Infrared sensors for aquatic pollutants : synthesis, optimization and qualification, Université de Rennes 1,, 2018.
[14] T. Kuriakose, Demonstration of the spatial self-trapping of a plasmonic wave, Bourgogne Franche-Comté, 2018.
[15] N. Sharma, S. Sharda, S.C. Katyal, V. Sharma, P. Sharma, Effect of Te on linear and non-linear optical properties of new quaternary Ge-Se-Sb-Te chalcogenide glasses, Electronic Materials Letters 10(1) (2014) 101-106.
[16] P.K. Singh, P. Lohia, D.K. Dwivedi, Investigation of dielectric relaxation and a.c. conductivity of third generation multi-component Ge10−xSe60Te30Sbx (0 ≤ x ≤ 6) chalcogenide glasses, Journal of Materials Science: Materials in Electronics 30(14) (2019) 13797-13809.
[17] H. Wang, T. Guo, Y. Xue, S. Lv, D. Yao, Z. Zhou, S. Song, Z. Song, The phase change memory features high-temperature characteristic based on Ge-Sb-Se-Te alloys, Materials Letters 254 (2019) 182-185.
[18] Y. Zhang, J.B. Chou, J. Li, H. Li, Q. Du, A. Yadav, S. Zhou, M.Y. Shalaginov, Z. Fang, H. Zhong, C. Roberts, P. Robinson, B. Bohlin, C. Ríos, H. Lin, M. Kang, T. Gu, J. Warner, V. Liberman, K. Richardson, J. Hu, Broadband transparent optical phase change materials for high-performance nonvolatile photonics, Nature Communications 10(1) (2019) 4279.
[19] G. Wang, Q. Nie, X. Wang, X. Shen, F. Chen, T. Xu, S. Dai, X. Zhang, New far-infrared transmitting Te-based chalcogenide glasses, Journal of Applied Physics 110(4) (2011) 043536.
[20] S. Zhang, X.-h. Zhang, M. Barillot, L. Calvez, C. Boussard, B. Bureau, J. Lucas, V. Kirschner, G. Parent, Purification of Te75Ga10Ge15 glass for far infrared transmitting optics for space application, Optical Materials 32(9) (2010) 1055-1059.
[21] F. Charpentier, M. Dussauze, M. Cathelinaud, G. Delaizir, E.I. Kamitsos, J.L. Adam, B. Bureau, V. Nazabal, Aging process of photosensitive chalcogenide films deposited by electron beam deposition, Journal of Alloys and Compounds 509(27) (2011) 7330-7336.
[22] R. Shuker, R.W. Gammon, Raman-Scattering Selection-Rule Breaking and the Density of States in Amorphous Materials, Physical Review Letters 25(4) (1970) 222-225.
[23] A.S. Ferlauto, G.M. Ferreira, J.M. Pearce, C.R. Wronski, R.W. Collins, X. Deng, G. Ganguly, Analytical model for the optical functions of amorphous semiconductors from the near-infrared to ultraviolet: Applications in thin film photovoltaics, Journal of Applied Physics 92(5) (2002) 2424-2436.
[24] E. Baudet, C. Cardinaud, A. Girard, E. Rinnert, K. Michel, B. Bureau, V. Nazabal, Structural analysis of RF sputtered Ge-Sb-Se thin films by Raman and X-ray photoelectron spectroscopies, Journal of Non-Crystalline Solids 444 (2016) 64-72.
[25] E. Baudet, M. Sergent, P. Němec, C. Cardinaud, E. Rinnert, K. Michel, L. Jouany, B. Bureau, V. Nazabal, Experimental design approach for deposition optimization of RF sputtered chalcogenide thin films devoted to environmental optical sensors, Scientific Reports 7(1) (2017) 3500.
[26] T.S. Moss, A Relationship between the Refractive Index and the Infra-Red Threshold of Sensitivity for Photoconductors, P Phys Soc Lond B 63(363) (1950) 167-176.
[27] M. Sheik-Bahae, E.W. Van Stryland, Semiconductors and Semimetals (Chapter 4), E. Garmire, A. Kost, San Diego, 1999
[28] J.B. Dory, C. Castro-Chavarria, A. Verdy, J.B. Jager, M. Bernard, C. Sabbione, M. Tessaire, J.M. Fédéli, A. Coillet, B. Cluzel, P. Noé, Ge–Sb–S–Se–Te amorphous chalcogenide thin films towards on-chip nonlinear photonic devices, Scientific Reports 10(1) (2020) 11894.

[29] K. Tanaka, Nonlinear optics in glasses: How can we analyze?, Journal of Physics and Chemistry of Solids 68(5) (2007) 896-900.
[30] T. Halenkovič, J. Gutwirth, T. Kuriakose, M. Bouška, M. Chauvet, G. Renversez, P. Němec, V. Nazabal, Linear and nonlinear optical properties of co-sputtered Ge-Sb-Se amorphous thin films, Opt. Lett. 45(6) (2020) 1523-1526.
[31] G. Lenz, J. Zimmermann, T. Katsufuji, M.E. Lines, H.Y. Hwang, S. Spalter, R.E. Slusher, S.W. Cheong, J.S. Sanghera, I.D.o.n. Aggarwal, Large Kerr effect in bulk Se-based chalcogenide glasses, Opt. Lett. 25(4) (2000) 254-256.
[32] V.G. Ta'eed, N.J. Baker, L. Fu, K. Finsterbusch, M.R.E. Lamont, D.J. Moss, H.C. Nguyen, B.J. Eggleton, D.Y. Choi, S. Madden, B. Luther-Davies, Ultrafast all-optical chalcogenide glass photonic circuits, Opt. Express 15(15) (2007) 9205-9221.
[33] T. Wang, X. Gai, W. Wei, R. Wang, Z. Yang, X. Shen, S. Madden, B. Luther-Davies, Systematic z-scan measurements of the third order nonlinearity of chalcogenide glasses, Opt. Mater. Express 4(5) (2014) 1011-1022.
[34] M. Dinu, Dispersion of phonon-assisted nonresonant third-order nonlinearities, IEEE Journal of Quantum Electronics 39(11) (2003) 1498-1503.
[35] P. Lucas, M.A. Solis, D.L. Coq, C. Juncker, M.R. Riley, J. Collier, D.E. Boesewetter, C. Boussard-Plédel, B. Bureau, Infrared biosensors using hydrophobic chalcogenide fibers sensitized with live cells, Sensors and Actuators B: Chemical 119(2) (2006) 355-362.
[36] F. Verger, V. Nazabal, F. Colas, P. Němec, C. Cardinaud, E. Baudet, R. Chahal, E. Rinnert, K. Boukerma, I. Peron, S. Deputier, M. Guilloux-Viry, J.P. Guin, H. Lhermite, A. Moreac, C. Compère, B. Bureau, RF sputtered amorphous chalcogenide thin films for surface enhanced infrared absorption spectroscopy, Opt. Mater. Express 3(12) (2013) 2112-2131.
[37] C. Gonçalves, R. Mereau, V. Nazabal, C. Boussard-Pledel, C. Roiland, E. Furet, M. Deschamps, B. Bureau, M. Dussauze, Study of the Ge20Te80-xSex glassy structures by combining solid state NMR, vibrational spectroscopies and DFT modelling, Journal of Solid State Chemistry 297 (2021) 122062.
[38] N. Abdellaoui, F. Starecki, C. Boussard-Pledel, Y. Shpotyuk, J.L. Doualan, A. Braud, E. Baudet, P. Nemec, F. Cheviré, M. Dussauze, B. Bureau, P. Camy, V. Nazabal, Tb3+ doped Ga5Ge20Sb10Se65-xTex (x = 0-37.5) chalcogenide glasses and fibers for MWIR and LWIR emissions, Opt. Mater. Express 8(9) (2018) 2887-2900.
[39] L. Petit, N. Carlie, K. Richardson, Y. Guo, A. Schulte, B. Campbell, B. Ferreira, S. Martin, Effect of the substitution of S for Se on the structure of the glasses in the system Ge0.23Sb0.07S0.70−xSex, Journal of Physics and Chemistry of Solids 66(10) (2005) 1788-1794.
[40] S. Sen, E.L. Gjersing, B.G. Aitken, Physical properties of GexAs2xTe100−3x glasses and Raman spectroscopic analysis of their short-range structure, Journal of Non-Crystalline Solids 356(41) (2010) 2083-2088.
[41] A. Mendoza-Galvan, E. Garcia-Garcia, Y.V. Vorobiev, J. Gonzalez-Hernandez, Structural, optical and electrical characterization of amorphous SeTe thin film alloys, Microelectron. Eng. 51-52 (2000) 677-687.
[42] I. Voleská, J. Akola, P. Jóvári, J. Gutwirth, T. Wágner, T. Vasileiadis, S.N. Yannopoulos, R.O. Jones, Structure, electronic, and vibrational properties of glassy Ga11Ge11Te78: Experimentally constrained density functional study, Physical Review B 86(9) (2012) 094108.
[43] G.C. Sosso, S. Caravati, R. Mazzarello, M. Bernasconi, Raman spectra of cubic and amorphous Ge2Sb2Te5 from first principles, Physical Review B 83(13) (2011) 134201.